RSC Advances

ROYAL SOCIETY OF CHEMISTRY

www.rsc.org/advances

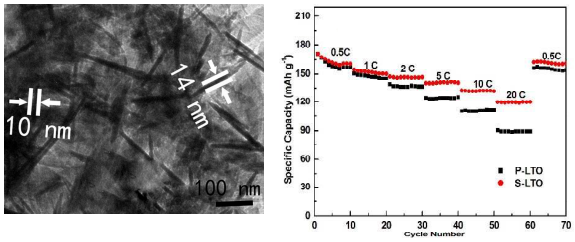

Ti^{3+} self-doped $Li_4Ti_5O1_2$ (S-LTO) nanosheets exhibit high specific capacity, excellent rate performance and outstanding cycling stability.

RSC Advances

RSCPublishing

ARTICLE

Ti^{3+} self-doped $Li_4Ti_5O_{12}$ nanosheets as anode materials for high performance lithium ion batteries

Cite this: DOI: 10.1039/x0xx00000x

Sen Nie, Chunsong Li, Hongrui Peng, Guicun Li* and Kezheng Chen*

Received 00th January 2012,
Accepted 00th January 2012

DOI: 10.1039/x0xx00000x

www.rsc.org/

Ti^{3+} self-doped $Li_4Ti_5O_{12}$ (S-LTO) nanosheets have been synthesized via a facile solvothermal approach combined with hydrogenation treatment. The thickness and lateral dimension of $Li_4Ti_5O_{12}$ nanosheets are 10–20 nm and 100–400 nm, respectively. The Ti^{3+} species and/or oxygen vacancies are well introduced into the crystal structures of $Li_4Ti_5O_{12}$ after hydrogen reduction, resulting into an enhancement in the electronic conductivity and the modified surface electrochemical activity. When evaluated for lithium storage capacity, the S-LTO nanosheets exhibit enhanced electrochemical energy storage performances compared to the pristine $Li_4Ti_5O_{12}$ (P-LTO) nanosheets, including high capacity (165.6 mA h g^{-1} at 0.5 C), excellent rate capability (119.6 mA h g^{-1} at 20 C), and good cyclic stability (95.3 % capacity retention after 100 cycles at 10 C). The improvement of lithium storage performances is ascribed to the increased electronic conductivity and the shortened lithium ion diffusion paths arising from the introduction of Ti^{3+} species and the ultrathin thickness of S-LTO.

Introduction

The development of high rate lithium ion batteries (LIBs) with high energy density and long cycle life is essential for the applications of LIBs in portable electronic devices.[1,2] In present conventional LIBs, graphite is a widely used anode material, but it has some disadvantages and can not gratifyingly meet the performance requirements of some important applications, especially in the safety and high rate performance.[3] It is demanding to develop alternative anode materials that can simultaneously meet the rate capability and safety requirements. In order to achieve this goal, a variety of Ti-based materials have been vividly investigated due to their high safety and excellent cycling stability.[4,5] Among them, spinel $Li_4Ti_5O_{12}$ (LTO) has been considered as one of the most promising anode materials for LIBs due to its long cycle life and remarkable reversibility.[6,7] LTO exhibits an badly flat discharge and charge plateaus at about 1.55 V (vs. Li/Li^+), which makes it safe by avoiding the solid electrolyte interface (SEI) formation.[8–10] Furthermore, LTO shows prominent reversibility due to its zero volume change during the charge-discharge cycles.[11,12] However, LTO is a poor electronic conductor (the conductivity is only 10^{-13} S cm^{-1}) and has a pacific lithium ion diffusion coefficient (10^{-9} to 10^{-13} cm^2 s^{-1}), which seriously limit its rate capability.[13–15]

Up till now, crucial efforts have been devoted to improving lithium ion storage kinetics and the electronic conductivity of LTO. One of the efficient methods is to tailor the size and morphology of LTO, which mainly improves its lithium ion storage kinetics due to the short electron and lithium ion diffusion path, and the enlarged contact area between the electrode and the electrolyte.[16–18] To date, miscellaneous morphological structures of LTO such as nanoflower hierarchical structures,[19–21] nanosheets,[22] nanotubes,[23] nanowires,[24] nanoparticles,[25,26] porous LTO microspheres,[27] etc. have been reported to modify the kinetic problems, which exhibit prominent electrochemical performances to different degrees. It is of interest that LTO nanosheets[22] are possible to present a pseudocapacitive effect as the interaction taking place on the surface, thus leading to an amelioration in the rate capability.[19,28] Another approach is to improve the electronic conductivity of the LTO electrode including surface coating methods,[29–33] doping ions or metals into a LTO lattice.[34–36] It has been reported that carbon-coated LTO,[29,30] rutile-TiO_2 nanocoated LTO,[31] and TiN-modified LTO,[32,33] exhibit better rate capability compared to the pristine LTO because of the introduction of extremely electronically conductive layers. Very recently, the introduction of oxygen vacancies and/or self-doping of Ti^{3+} into the metal oxides have proved to be a promising avenue to manipulate and fundamentally improve their optical and electronic properties.[37–43] For examples, Lu et al.[40] have prepared hydrogenated TiO_2 nanotube arrays with enhanced electronic conductivity, which show substantially improved electrochemical performance for supercapacitors. Our group have reported that both hydrogenated TiO_2(B) nanostructures and mesoporous hydrogenated anatase TiO_2 microspheres exhibited enhanced high-rate capability due to their improved electronic conductivity.[37,43] Cao et al.[42] have fabricated hydrogenated LTO nanowire arrays growing directly on Titanium foil with excellent rate capability. As reported previously,[38] partial reduction of Ti^{4+} by lithiation can improve electronic conductivity of LTO, which is favorable for the development of carbon-free electrode materials. The facile hydrogenation of LTO for high electronic conductivity may take the place of conventional carbon

coating, which is desired for the mass production. Herein, we report the synthesis of S-LTO nanosheets as anode materials for LIBs by a facile solvothermal method combined with hydrogenation treatment process. As expected, the S-LTO electrodes exhibit enhanced electrochemical properties, especially better rate capability, compared to the P-LTO electrodes.

Experimental

Synthesis of the LTO precursor

All reagents were used without further purification. The LTO precursor was synthesized by a simple hydrothermal method. In a typical synthesis process, 0.394 g LiOH·H_2O was dissolved in 60 mL water and then 2 mL of butyl titanate was slowly added dropwise to the aqueous solutions of LiOH. The solution was kept stirring for 2 h, then transferred into a 80 mL Teflon-lined autoclave and maintained at 180 ℃ for 20 h. After it cooled to room temperature naturally, the resulting white precipitate was recovered, washed with deionized water and ethanol for several times by centrifugation, and then dried in an oven at 80 ℃.

Synthesis of P-LTO nanosheets

The precursor $Li_{1.81}H_{0.19}Ti_2O_5 \cdot xH_2O$ nanosheets was put into an tubular furnace and calcined at 500 ℃ for 2 h in air with a heating rate of 3 ℃ min^{-1}. P-LTO nanosheets were successfully synthesized after the furnace was cooled down to room temperature.

Synthesis of S-LTO nanosheets

The P-LTO nanosheets were put into a tubular furnace filled with static hydrogen atmosphere. The hydrogen thermal treatment was performed by calcining the P-LTO nanosheets at 500 ℃ for 2 h with a heating rate of 3 ℃ min^{-1}. The S-LTO nanosheets were obtained after the furnace was completely cooled down to room temperature.

Characterization

The crystal structures of the samples were analyzed by X-ray diffraction (XRD Rigaku D-max-γA XRD with Cu kα radiation, λ=1.54178 Å) from 10 ° to 80 °. The morphologies and sizes of the samples were characterized using field-emission scanning electron microscopy (FE-SEM, JSM 6700F) and transmission electron microscopy (TEM, FEI Tecnai G20). The X-ray photoelectron spectroscopy (XPS) analysis was performed on a Perkin-Elmer PHI 550 spectrometer with Al Ka (1486.6 eV) as the X-ray source.

Electrochemical test

The electrochemical measurements were carried out using a CR2032-type coin cell at room temperature. A slurry was prepared by mixing 70 wt % the samples, 20 wt % carbon black (Super-P), and 10 wt % poly(vinyl difuoride) (PVDF) as binder and a certain amount of N-methylpyrrolidinone (NMP) as solvent. The mixed slurry was coated uniformly onto pure Cu foil, dried in air and subsequently dried in vacuum at 120 ℃ for 12 h. Pure lithium foil was used as the counter electrode and separated using a Celgard 2500 membrane separator. The electrolyte consisted of a solution of 1 mol L^{-1} $LiPF_6$ in ethylene carbonate-dimethyl carbonate (1:1 by volume). The cells were assembled in a glove box filled with high purity argon gas. The galvanostatic discharge-charge experiments were performed over a voltage range of 1.0–3.0 V (vs. Li^+/Li) at different rates using a LAND CT2001A battery tester. Electrochemical impedance spectroscopy (EIS) measurements were carried out on an Autolab PGSTAT302N electrochemical workstation by applying a sine wave with an amplitude of 10.0 mV over the frequency range from 100 kHz to 10 mHz. Cyclic voltammetry (CV) curves were obtained using the same workstation as EIS measurements at a scanning rate of 0.5 mV s^{-1}.

Results and discussion

Fig. 1a shows the XRD pattern of the LTO precursor. All the diffraction peaks of various planes can be well indexed to the orthorhombic $Li_{1.81}H_{0.19}Ti_2O_5 \cdot xH_2O$ (JCPDS card No. 47-0123). The diffraction peaks are broad possibly due to the low crystallinity of the $Li_{1.81}H_{0.19}Ti_2O_5 \cdot xH_2O$ precursor. The XRD patterns of the S-LTO nanosheets and P-LTO nanosheets shown in Fig. 1b reveal the standard peaks of spinel LTO (PDF no. 49-0207). No impurity is detected, indicating that the layered $Li_{1.81}H_{0.19}Ti_2O_5 \cdot xH_2O$ precursor has been completely transformed into spinel LTO. The sharp diffraction peaks suggest the high crystallinity of the S-LTO nanosheets and P-LTO nanosheets. Moreover, the crystal phase of LTO is not affected greatly by the hydrogen reduction process.

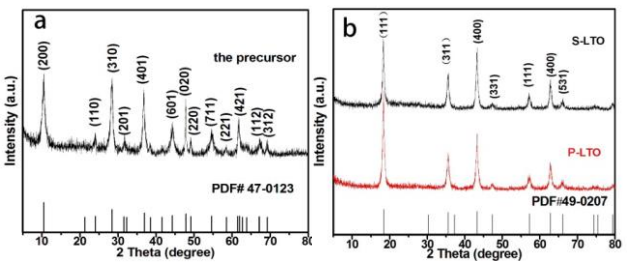

Fig. 1 XRD patterns of the LTO precursors (a), P-LTO nanosheets and S-LTO nanosheets (b).

The sizes and morphologies of S-LTO and P-LTO nanostructures are characterized by the SEM, TEM, and HRTEM analysis. SEM images (Fig. 2a and b) show that both the P-LTO nanosheets and S-LTO nanosheets consists of standing and spreading two-dimensional sheets with irregular quadrilateral shapes. The thickness and lateral dimension of LTO nanosheets are 10–20 nm and 100–400 nm, respectively. The sheetlike morphology of both samples can be further confirmed by the corresponding TEM images shown in Fig. 2c and d. It is found that the LTO nanosheets are independent of each other, without any stacking or assembling phenomenon. The thickness of the S-LTO nanosheets is similar to that of the P-LTO nanosheets, revealing that the regrowth of LTO does not happen during the hydrogen treatment process. HRTEM images

of the S-LTO nanosheets (Fig. 2f) and P-LTO nanosheets (Fig. 2e) show that the lattice spacings of 0.48 nm, corresponding to the lattice spacings the (111) planes of spinel LTO.

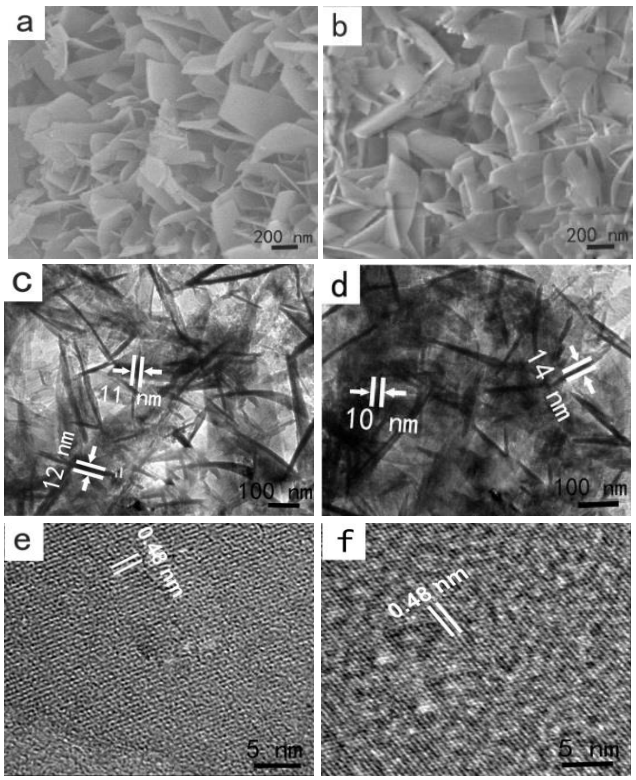

Fig. 2 SEM (a), TEM (c) and HRTEM (e) images of P-LTO nanosheets. SEM (b), TEM (d) and HRTEM (f) images of S-LTO nanosheet.

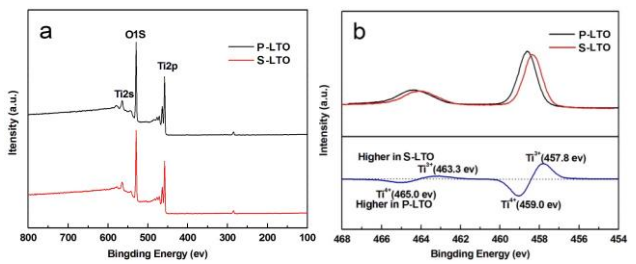

Fig. 3 XPS survey spectra of the S-LTO and P-LTO nanosheets (a) and normalized Ti 2p core level XPS spectra of S-LTO and P-LTO nanostructures together with their difference spectrum (b).

XPS analysis was performed to examine the effect of hydrogenation on the chemical composition and oxidation state of LTO nanosheets. Fig. 3 shows the XPS survey spectra of the S-LTO and P-LTO nanosheets. It can be clearly seen that both the S-LTO and P-LTO nanosheets show the similar sharp and peak intensity, indicating their high purity (Fig. 3a). The upper panel of Fig. 3b shows the normalized Ti 2p core level XPS spectra of the S-LTO and P-LTO nanosheets. From the spectra of P-LTO nanosheets, two broad peaks centered at 465.0 and 459.0 eV are observed, which correspond to the characteristic Ti $2p_{1/2}$ and Ti $2p_{3/2}$ peaks of Ti^{4+} species, respectively.[44–47] In comparison with P-LTO, the peaks of the S-LTO sample show a negative shift in binding energy, indicating that it has different bonding environments. By subtracting the normalized Ti 2p spectra of S-LTO with P-LTO sample (lower panel of Fig. 3b), two extra peaks centered at ca. 463.3 and 457.8 eV are observed, which are consistent with the characteristic Ti $2p_{1/2}$ and Ti $2p_{3/2}$ peaks of Ti^{3+} species, respectively.[48,49] These results confirm the presence of Ti^{3+} species in the S-LTO nanosheets and oxygen vacancies (Ti^{3+} sites) are created in the S-LTO nanosheets during the hydrogen reduction process.

To investigate the influences of hydrogenation on the electrochemical properties of LTO, the CV, galvanostatic discharge-charge, and EIS tests were performed and evaluated in lithium half-cells. Fig. 4a compares the CV curves of the S-LTO and at a scanning rate of 0.1 mV s^{-1} in the potential window of 1.0–3.0 V (vs. Li^+/Li). It should be noted that the peaks of S-LTO was sharper and intense, and the gap between redox peaks was smaller than that of P-LTO, demonstrating that the former exhibits better electrode kinetics, preferable reversibility due to a lower degree of polarization of the electrodes during the electrochemical reaction and greater efficiency of the redox reaction. Fig. 4b shows the typical charge and discharge profiles of the S-LTO electrode cycled at different current rates from 0.5 C to 20 C in the potential range of 1.0–3.0 V. It delivers a reversible discharge capacity of 165.6 mA h g^{-1} at the initial lower rate of 0.5 C, which is close to theoretical capacity of 175 mA h g^{-1}. Furthermore, the electrode shows a flat discharge plateau at the potential of 1.55 V, which is ascribed to the redox reaction of Ti^{4+}/Ti^{3+}. As the charge-discharge rate increases from 1 C to 10 C, the discharge capacity of the S-LTO electrode is slightly decreased, and it delivers 155.4, 147.8, 142.1, and 134.2 mA h g^{-1} at a rate of 1, 2, 5, and 10 C, respectively. Even at a high rate of 20 C, the S-LTO electrode exhibits a high capacity of 119.6 mA h g^{-1} with capacity retention as high as 72.2% of the value achieved at 0.5 C, indicating the excellent rate capability of the S-LTO electrode material. However, as shown in Fig. 4c, the P-LTO electrode delivers discharge capacities of 154.6, 150.3, 139.1, 128.3, 114.3, and 94.3 mA h g^{-1} at a rate of 0.5, 1, 2, 5, 10, and 20 C, respectively. Obviously, the S-LTO electrode displays a much higher capacity at various rates. In addition, the potential gap between the charge and discharge plateaus of the S-LTO electrode is 0.52 V at a rate of 20 C, which is much smaller than that of the P-LTO electrode (0.77 V), demonstrating that the former exhibits better electrode kinetics due to a lower degree of polarization. Fig. 4d compares the rate capability of the S-LTO and P-LTO electrodes. It is found that the storage capacities of both electrodes are stable at each current rate. When the current rate reverses back to 0.5 C, their cell capacities can recover to the original value immediately, indicating that the electrode materials possess high structure stability even after high rate cycling. Fig. 4e gives the long-term cycling performance and the Coulombic efficiency of the S-LTO and P-LTO electrodes at a high current rate of 10 C. In the case of the hydrogenated sample, the initial capacity is 136.5 mA h g^{-1}, which decreases to 130.1 mA h g^{-1} after 100

cycles, with a good capacity retention of 95.3 %. However, for the pristine sample, the initial capacity is 116.3 mA h g^{-1}, which decreases to 108.5 mA h g^{-1} after 100 cycles, with an inferior capacity retention of 93.3 %. The introduction of Ti^{3+} species and/or oxygen vacancies greatly improves the electronic conductivity, resulting into the improvement of initial Columbic efficiency is significant for S-LTO. It should be noted that he Coulombic efficiency of both S-LTO and P-LTO electrodes is maintained almost 100% apart from the seventh several cycles.

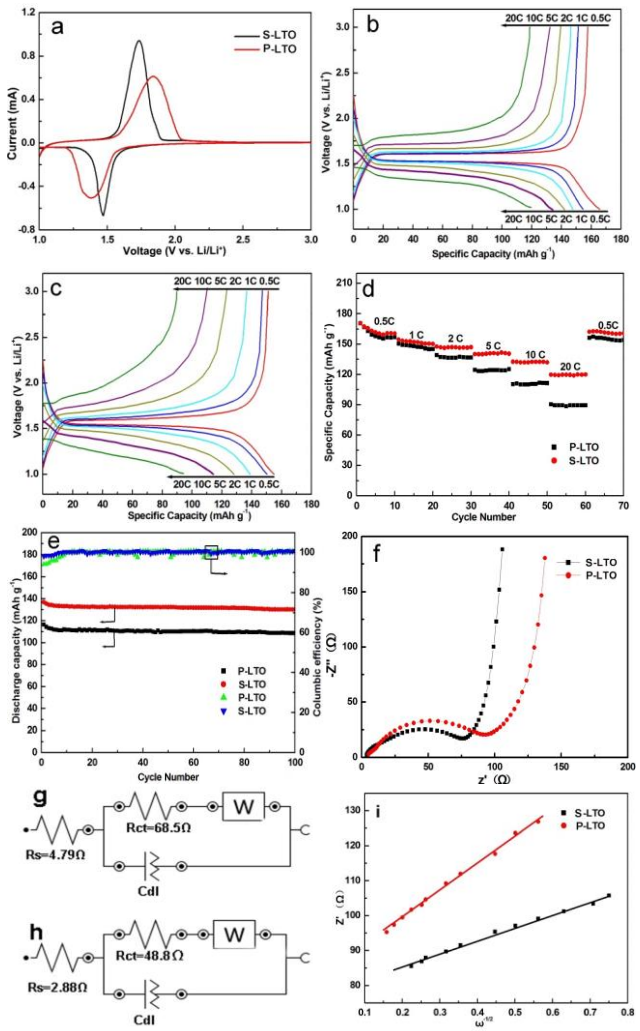

Fig. 4 (a) CV curves of S-LTO and P-LTO electrodes at a scan rate of 0.1 mV s^{-1}. Galvanostatic discharge-charge profiles of S-LTO electrode (b) and P-LTO electrode (c) at various rates. (d) Comparison of the rate performance of S-LTO electrode and P-LTO electrode. (e) The long-term cycling performances and the Coulombic efficiencies of S-LTO and P-LTO electrodes at 10 C. (f) Complex impedance plots at room temperature for S-LTO and P-LTO nanosheets. Equivalent circuits for the P-LTO electrode (g) and S-LTO electrode (h). (i) The relation of Z' (real) and $\omega^{-1/2}$ at low frequency.

Fig. 4f shows the EIS curves of fresh cells at discharge states at room temperature. Each of the curves consists of a straight line (at low frequency) and a depressed semicircle (at high frequency), which are related to the lithium ion diffusion in the bulk of the electrode and the charge transfer process at the electrolyte–electrode interface, respectively. The EIS spectra fitted using equivalent circuits of the P-LTO and S-LTO electrodes are shown in Fig. 4g and h, respectively. It can also be seen that the S-LTO exhibits a much lower Rct value (48.8 Ω) than that of the P-LTO electrode (68.5 Ω), mainly due to mainly due to the enhanced electronic conductivity after the introduction of oxygen vacancies and/or Ti^{3+} species into the LTO nanostructures. In addition to Rct, the apparent lithium ion diffusion coefficient (D_{Li}) also has a noticeable synergistic effect. The values of D_{Li} are calculated from the inclined lines in the Warburg region in lower frequency ranges, based on the following equation: $D_{Li} = R^2T^2/2A^2n^4F^4C^2\sigma^2$, or where R is the gas constant, T is the absolute temperature, A is the surface area of the anode electrode, n is the number of electrons per molecule during oxidization, F is the Faraday constant, C is the lithium concentration and σ is the Warburg factor. The Warburg factors s for both electrodes are determined by plotting in the complex plane $-Z'$ (real) $= \sigma \times \omega^{-1/2}$ against $\omega^{-1/2}$ where ω is the angular frequency, which are presented in Fig. 4i The D_{Li} value of the S-LTO electrode is calculated to be 1.35×10^{-12} cm^2 s^{-1}, which is about five times higher than that of P-LTO electrode (2.9×10^{-13} cm^2 s^{-1}). The excellent rate capability of S-LTO electrode is attributed to the enhanced electronic conductivity and the modified surface electrochemical activity after introducing oxygen vacancies (Ti^{3+} species) and hydroxyl groups into the LTO nanostructures.

Conclusions

In conclusion, we have employed a combined solvothermal and hydrogenation treatment process to successfully synthesize hydrogenated LTO nanosheets. The introduction of Ti^{3+} species and/or oxygen vacancies greatly improves the electronic conductivity. As expected, the S-LTO nanostructures exhibit improved lithium ion storage performance including higher specific capacity, superior rate performance, and better cycling stability in comparison with the P-LTO nanostructures. The facile hydrogenation method can be expected to open up opportunities in designing high-performance carbon-free electrode materials with semiconductor features for lithium ion batteries.

Acknowledgements

This work was supported by the National Natural Science Foundation of China (51272113).

Notes and references

Laboratory of Functional and Biological Nanomaterials, College of Materials Science and Engineering, Qingdao University of Science and Technology, Qingdao 266042, China. To whom correspondence should be addressed. Tel: 86-532-84022814. Fax: 86-532-84022814. E-mail: guicunli@qust.edu.cn and kchen@qust.edu.cn.

1 J. M. Tarascon and M. Armand, *Nature*, 2001, **414**, 359.

2 B. Dunn, H. Kamath and J. M. Tarascon, *Science*, 2011, **334**, 928.

3 M. Endo, C. Kim, K. Nishimura, T. Fujino and K. Miyashita, *Carbon*, 2000, **38**, 183.
4 G. N. Zhu, Y. G. Wang and Y. Y. Xia, *Energy Environ. Sci*., 2012, **5**, 6652.
5 Z. Hong and M. Wei, *J. Mater. Chem. A*, 2013, **1**, 4403.
6 K. Zaghib, M. Armand and M. Gauthier, *J. Electrochem. Soc*., 1998, **145**, 135.
7 K. M. Colbow, J. R. Dahn and R. R. Haering, *J. Power Sources*, 1989, **26**, 397.
8 G. G. Amatucci, F. Badway, A. D. Pasquier, T. Zheng, *J. Electrochem. Soc*., 2001, **148**, 930.
9 L. Yu, H. B. Wu and X. W. Lou, *Adv. Mater*., 2013, **25**, 2296.
10 L. F. Shen, X. G. Zhang, H. S. Li, C. Z. Yuan, G. Z. Cao, *J. Phys. Chem. Lett*. 2011, **2**, 3096.
11 T. Ohzuku, A. Ueda and N. Yamamota, *J. Electrochem. Soc*., 1995, **142**, 1431.
12 A. S. Prakash, P. Manikandan, K. Ramesha, M. Sathiya, J. M. Tarascon and A. K. Shukla, *Chem. Mater*., 2010, **22**, 2857.
13 A. S. Aric`o, P. Bruce, B. Scrosati, J. M. Tarascon and W. V. Schalkwijk, *Nat. Mater*., 2005, **4**, 366.
14 B. Zhang, Y. Liu, Z. Huang, S. Oh, Y. Yu, Y. W. Mai and J. K. Kim, *J. Mater. Chem*., 2012, **22**, 12133.
15 J. Haetge, P. Hartmann, K. Brezesinski, J. Janek and T. Brezesinski, *Chem. Mater*., 2011, **23**, 4384.
16 L. Yu, H. B. Wu and X. W. Lou, *Adv. Mater*., 2013, **25**, 2296.
17 P. G. Bruce, B. Scrosati and J. M. Tarascon, *Angew. Chem., Int. Ed*., 2008, **47**, 2930.
18 J. M. Feckl, K. Fominykh, M. Dolinger, D. F. Rohlng and T. Bein, *Angew. Chem., Int. Ed*., 2012, **51**, 7459
19 G. Hasegawa, K. Kanamori, Y. Sugawara, Y. Ikuhara and K. Nakanishi, *J. Colloid Interface Sci*., 2012, **374**, 291.
20 Y. S. Lin, M. C. Tsai and J. G. Duh, *J. Power Sources*, 2012, **214**, 314.
21 J. Liu, X. F. Li, J. L. Yang, D. S. Geng, Y. L. Li, D. N. Wang, R. Y. Li, X. L. Sun, M. Cai and M. W. Verbrugge, *Electrochim. Acta*, 2012, **63**, 100.
22 C. Lai, Y. Y. Dou, X. Li and X. P. Gao, *J. Power Sources*, 2010,**195**, 3676.
23 S. C. Lee, S. M. Lee, J. W. Lee, J. B. Lee and S. M. Lee, *J. Phys. Chem. C*, 2009, **113**, 18420.
24 D. K. Lee, H.W. Shim, J. S. An, C. M. Cho, I. S. Cho, K. S. Hong and D. W. Kim, *Nanoscale Res. Lett*., 2010, **5**, 1585.
25 A. Nugroho, S. J. Kim, K. Y. Chung and J. Kim, *Electrochim Acta*, 2012, **78**, 623.
26 A. Nugroho, S. J. Kim, K. Y. Chung, B. W. Cho, Y. W. Lee and J. Kim, *Electrochem. Commun*., 2011, **13**, 650.
27 L. Shen, C. Yuan, H. Luo, X. Zhang, K. Xu and Y. Xia, *J. Mater. Chem*., 2010, **20**, 6998
28 L. Kavan, M. Kalbac, M. Zukalova, I. Exnar, V. Lorenzen,R. Nesper and M. Graetzel, *Chem. Mater*., 2004, **16**, 477.
29 G. N. Zhu, H. J. Liu, J. H. Zhuang, C. X. Wang, Y. G. Wang and Y. Y. Xia, *Energy Environ. Sci*., 2011, **4**, 4016.
30 E. Kang, Y. S. Jung, G. H. Kim, J. Chun, U. Wiesner, A. C. Dillon, J. K. Kim and J. Lee, *Adv. Funct. Mater*., 2011,**21**, 4349.
31 K. S. Park, A. Benayad, D. J. Kang and S. G. Doo, *J. Am. Chem. Soc*., 2008, **130**, 14930.
32 Y.Q.Wang, L. Gu, Y. G. Guo, H. Li, X. Q. He, S. Tsukimoto, Y. Ikuhara and L. J. Wan, J. *Am. Chem. Soc*., 2012, **134**, 7874
33Y. Zhao, S. Pang, C. Zhang, Q. Zhang, L. Gu, X. Zhou, G. Li and G. Cui, *J. Solid State Electrochem*., 2013, **17**, 1479.
34 C. C. Li, Q. H. Li, L. B. Chen and T. H. Wang, *ACS Appl. Mater. Interfaces*, 2012, **4**, 1233.
35 T. F. Yi, Y. Xie, L. J. Jiang, J. Shu, C. B. Yue, A. N. Zhou and M. F. Ye, *RSC Adv*., 2012, **2**, 3541.
36 Y. J. Bai, C. Gong, N. Lun and Y. X. Qi, *J. Mater. Chem. A*, 2013, **1**, 89.
37 G. Li, Z. Zhang, H. Peng and K. Chen, *RSC Adv.*, 2013, **3**, 11507.
38 M. S. Song, A. Benayad, Y. M. Choi and K. S. Park, *Chem. Commun.*, 2012, 48, 516.
39 X. Lu, G. Wang, T. Zhai, M. Yu, J. Gan, Y. Tong and Y. Li, *Nano Lett*., 2012, **12**, 1690.
40 X. Chen, L. Liu, P. Y. Yu and S. S. Mao, *Science*, 2011, **331**, 746.
41 J. Y. Shin, J. H. Joo, D. Samuelis, J. Maier, *Chem. Mater.*, 2012, **24**, 543.
42 L. Shen, E. Uchaker, X. Zhang and G. Cao, *Adv. Mater*., 2012, 24, 6502.
43 Z. Zhang, Z. Zhou, S. Nie, H. Wang, H. Peng, G. Li and K. Chen, *J. Power Sources*, 2014, **267**, 388.
44 S. T. Myung, M. Kikuchi, C. S. Yoon, H. Yashiro, S. J. Kim, Y. K. Sun and B. Scrosati, *Energy Environ. Sci*., 2013, **6**, 2609.
45 X. Jiang, Y. Zhang, J. Jiang, Y. Rong, Y. Wang, Y. and Wu, C. Pan, *J. Phys. Chem. C*, 2012, **116**, 22619.
46 A. Naldoni, M. Allieta, S. Santangelo, M. Marelli, F. Fabbri, S. Cappelli, C. L. Bianchi, R. Psaro and V. D. Santo, *J. Am. Chem. Soc*., 2012, **134**, 7600.
47 M. S. Lazarus, T. K. Sham, *Chem. Phys. Lett*., 1982, **92**, 670.
48 F. Werfel and O. Brummer, *Phys. Scr*., 1983, **28**, 92.
49 E. McCafferty and J. P. Wightman, *Surf. Interface Anal*., 1998, **26**, 549